

Coexistence of Weyl fermion and massless triply degenerate nodal points

Hongming Weng,^{1,2,*} Chen Fang,^{1,†} Zhong Fang,^{1,2} and Xi Dai^{1,2}

¹Beijing National Laboratory for Condensed Matter Physics, and Institute of Physics, Chinese Academy of Sciences, Beijing 100190, China

²Collaborative Innovation Center of Quantum Matter, Beijing, China

(Received 24 May 2016; published 6 October 2016)

By using first-principles calculations, we propose that WC-type ZrTe is a new type of topological semimetal (TSM). It has six pairs of chiral Weyl nodes in its first Brillouin zone, but it is distinguished from other existing TSMs by having an additional two pairs of massless fermions with triply degenerate nodal points as proposed in the isostructural compounds TaN and NbN. The mirror symmetry, threefold rotational symmetry, and time-reversal symmetry require all of the Weyl nodes to have the same velocity vectors and locate at the same energy level. The Fermi arcs on different surfaces are shown, which may be measured by future experiments. It demonstrates that the “material universe” can support more intriguing particles simultaneously.

DOI: [10.1103/PhysRevB.94.165201](https://doi.org/10.1103/PhysRevB.94.165201)

I. INTRODUCTION

Different types of topological semimetals (TSMs) have been proposed and studied intensively in recent years [1–4]. All these TSMs can be classified according to the different band crossing points at the Fermi level and the mechanism protecting them. For example, Dirac semimetal (DSM) [5–7] can be either protected by special crystalline symmetries on high symmetrical crystal momentum points or along high symmetry lines [8], and Weyl semimetal (WSM) [9–20] can be stabilized without any additional crystalline symmetry besides the lattice translation. Exotic surface states forming open “Fermi arcs” [6,10,11] and negative magnetoresistance [21–23] caused by “chiral anomaly” are two important physical consequences of Dirac and Weyl semimetal states. Very recently, another class of TSM materials characterized by three- or sixfold band crossings have been proposed to have “new fermions” with quite interesting physical properties discussed in Refs. [24–26].

In the present paper we propose that ZrTe is a material that hosts both the new fermion state with triply degenerate crossing points and the Weyl fermion state near the Fermi energy. ZrTe has the same crystal structure and similar band structure along the Γ -A direction with TaN, which has triply degenerate nodes [26]. While what is new in ZrTe is that at the same time the band structure of ZrTe also contains six pairs of Weyl points near the mirror plane of $k_z = 0$. The microscopic mechanism for the formation of the Weyl points in ZrTe is similar to TaAs [12], where the non-spin-orbit coupled (SOC) band structure contains nodal lines on the mirror plane. Turning on SOC leads to the disappearance of the nodal lines on the mirror plane and the appearance of Weyl nodes off the plane. Compare to TaAs, an important advantage for the WSM phase in ZrTe is that all the Weyl points are related by crystalline symmetry D_{3h} , so that all of them are located at the same energy. Regarding the surface states, an interesting point in ZrTe as a WSM is that there are four different symmetric Fermi arc patterns allowed by symmetry on the (001) surfaces

and fruitful surface Lifshitz transitions may be induced by changing the surface condition accordingly.

II. COMPUTATIONAL DETAILS

The software package OpenMX [27] is employed for most of the first-principles calculations, which is based on the linear combination of pseudoatomic orbitals [28]. The local orbital basis sets for Zr and Te are chosen as Zr9.0- $s2p2d2f1$ and Te7.0- $s2p2d1$, respectively. The experimental crystal structure of WC-type ZrTe has been studied by Örylgsson *et al.* [29,30] and is fully relaxed until the residual forces on each atom is less than 0.001 eV/Å. The sampling of the Brillouin zone in the self-consistent process is taken as the grid of $12 \times 12 \times 10$. Exchange-correlation potential is treated within the generalized gradient approximation (GGA) of Perdew-Burke-Ernzerhof type [31]. The possible underestimation of band gap within GGA is checked by a nonlocal Heyd-Scuseria-Ernzerhof (HSE06) hybrid functional [32,33] calculation using VASP software package [34,35]. SOC is taken into account self-consistently in both software packages. The maximally localized Wannier functions (MLWF) [36,37] for the d orbitals of Zr are generated by using OpenMX [38]. Then, a tight-binding model based on these has been established to calculate the surface states with the Green's function methodology [39,40].

III. RESULTS AND DISCUSSION

Crystal structure. As shown in Fig. 1, the WC-type ZrTe has the same crystal structure as θ -TaN [41,42] and NbN [43,44]. Hereafter we will simply call them ZrTe, TaN, and NbN, respectively. The space group is $P\bar{6}m2$ (No. 187). Zr and Te atoms occupy the $1d$ ($1/3, 2/3, 1/2$) and $1a$ (0,0,0) Wyckoff positions, respectively. The experimental lattice constants are $a = b = 3.7707$ Å and $c = 3.8606$ Å. The optimized lattice constants are $a = b = 3.7966$ Å and $c = 3.9003$ Å, being slightly overestimated by 1.0%. All the results discussed in the following are from the calculations with optimized ones.

Band structure of ZrTe. The band structure calculated within GGA is shown in Fig. 2. When compared with that of TaN [26], the band crossings along Γ -A between d_{z^2} and

*hmweng@iphy.ac.cn

†cfang@iphy.ac.cn

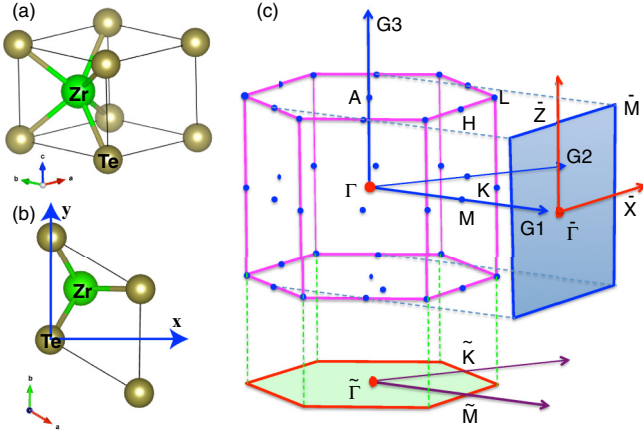


FIG. 1. (a) The crystal structure of WC-type ZrTe and (b) the top view. (c) The bulk Brillouin zone and its projection onto the (100) and (001) surfaces. The high symmetrical crystal momenta are indicated with letters.

$d_{x^2-y^2} + d_{xy}$ bands are the same. The energy dispersions along A-L-H-A within $k_z = \pi$ plane are also the same. The most distinct difference is within the $k_z = 0$ plane, where additional band inversion around K happens in ZrTe but is absent in TaN. Such band inversion includes $d_{x^2-y^2} + d_{xy}$ and $d_{xz} + d_{yz}$ bands. Since $k_z = 0$ plane is a mirror plane and the two bands have opposite mirror eigenvalue, the band inversion leads to a circle of node-line centering K point, which is similar to the case in TaAs [12]. The hybrid functional calculation is used to overcome the possible overestimation of band inversion in GGA. The comparison of them is shown in Fig. 2(b),

which indicates that these two band inversions occur in both cases.

With SOC being included, the bands in Figs. 3(a) and 3(b) along Γ -A cross at two triply degenerate nodal points (TDNPs), which are the massless fermions discussed in TaN and NbN [26]. However, the additional band inversion around K results in six pairs of Weyl nodes in its first Brillouin zone (BZ). Since the properties associated with the TDNP have already been discussed in detail in our previous paper on TaN and NbN, in this work we mainly focused on the properties related to the existence of Weyl points, which is absent in TaN or NbN.

As shown in Fig. 3(c), the lack of inversion symmetry leads to Rashba-like spin splitting in the bands along M - K - Γ . The node lines around both K and K' (time-reversal partner of K) within GGA in Fig. 4(a) are fully gapped, but each of them will lead to three pairs of Weyl nodes off the $k_z = 0$ mirror plane and will be discussed later. Since the electronic states in both the $k_z = 0$ and $k_z = \pi$ planes can be looked as two-dimensional (2D) “insulators” with time-reversal symmetry, the band topology can be identified by Z_2 numbers. Here we use insulators to mean that at each k point there is finite energy gap between the blue and red bands shown in Fig. 3(c). Thus, the Z_2 number is well defined for all bands below the red one though it is metallic with Fermi pockets at the chemical potential indicated by the dashed line. The Wilson loop method [39,40,45] is used to calculate the evolution of the “Wannier centers” formed along the k_y direction. It is found that in both planes the Z_2 numbers are odd [see Figs. 3(d) and 3(e)]. Compared to the situation in TaN, we note that here both the $k_z = 0$ and $k_z = \pi$ planes are topologically nontrivial, whereas in TaN only the $k_z = \pi$ plane is nontrivial.

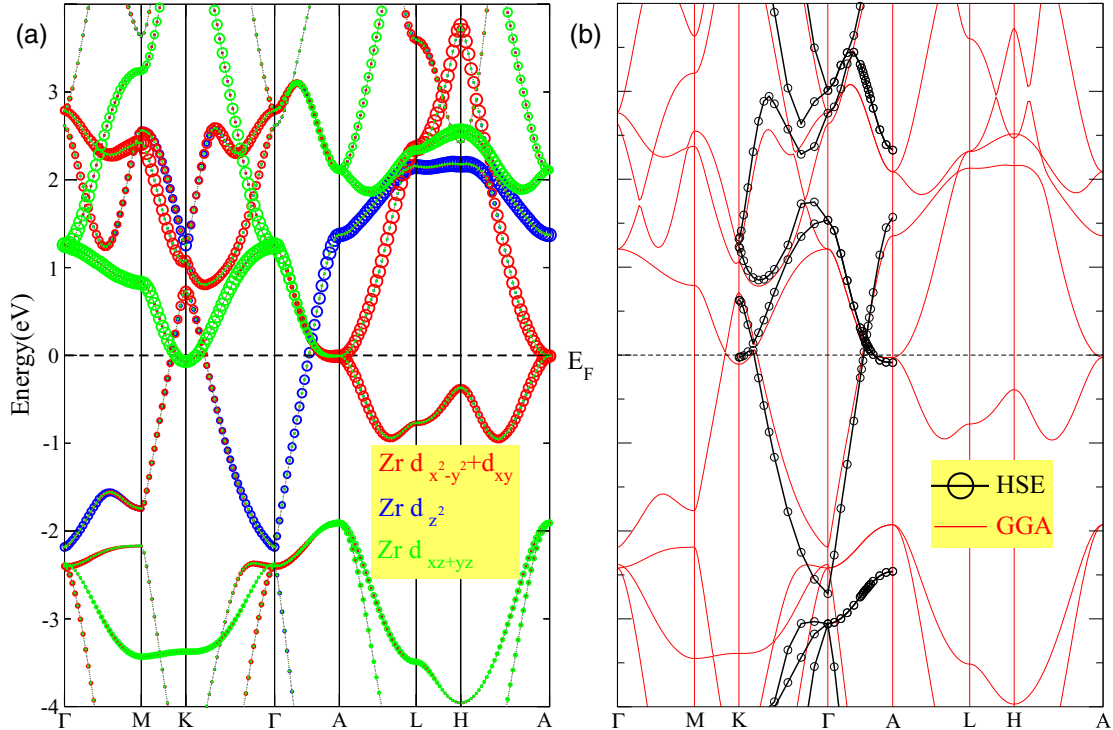


FIG. 2. Band structure of ZrTe without SOC. (a) The fatted bands with spectral weight of Zr d_{z^2} , $d_{x^2-y^2} + d_{xy}$, and $d_{xz} + d_{yz}$ orbitals. (b) The band structures calculated within GGA (lines) and hybrid functional HSE06 (circled lines).

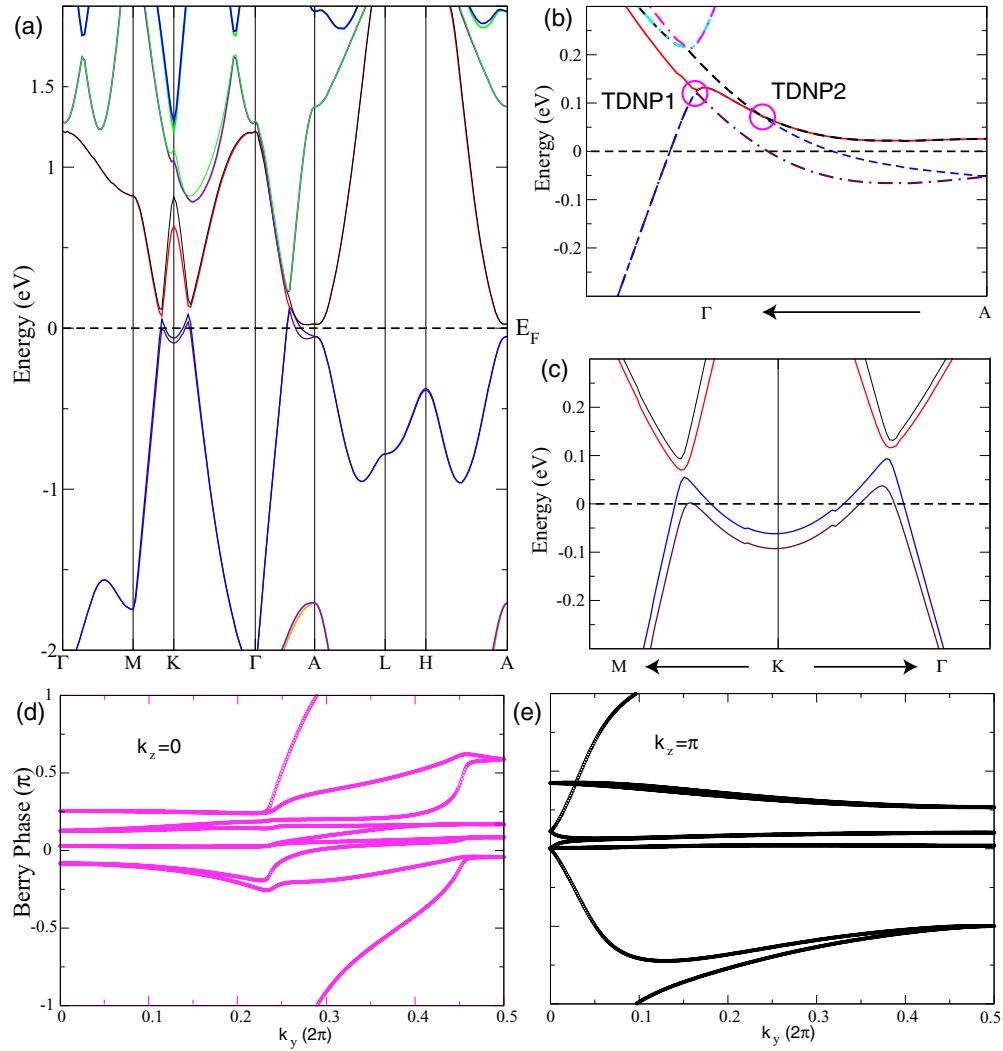


FIG. 3. (a) Band structure with SOC included. (b) Enlarged band structure along M - K - Γ and (c) Γ - A in (a). (d) The k_y evaluation of Berry phases of occupied bands in k_x periodicity in $k_z = 0$ and (e) $k_z = \pi$ plane for ZrTe.

Weyl nodes in ZrTe. By first-principle calculations, we have located the positions of all the WPs in ZrTe, which are shown in Fig. 4(a) from the top view along the c axis. In total there are six pairs of WPs in the BZ with half of them being above and the other half being below the $k_z = 0$ plane. Due to the high crystalline symmetry in ZrTe, all the WPs can be related to each other by the C_3 rotation, the vertical mirror ΓMA , and the horizontal mirror ΓMK . Therefore all the WPs are located at the same energy similar to the situation in strained HgTe [46] or chalcopyrites [47]. One typical pair of WPs are located at $(0.26984, 0.26984, \pm 0.00655)$ in unit of reciprocal lattice vectors.

When these Weyl nodes are projected onto (100) surfaces, the different chiral Weyl nodes are projected onto a different position as shown in Fig. 4(b) and there are two pairs superposed, each other indicated with bigger circles labeled as W2. Others are W1. When they are projected onto the (010) surface, the Weyl nodes with opposite chirality are superposed as shown in Fig. 4(c), which is similar for the (001) surface. The Dirac conelike band structures passing through one of the

Weyl node is plotted along Γ - K and z axis in Figs. 4(d) and 4(e), respectively. The Weyl node is located at 50 meV above the Fermi level.

Surface states of ZrTe. In the main text we will focus on the (001) surface states. Those on the side surfaces (100) and (010) are shown and briefly discussed in Appendixes A and B, respectively. On the (001) surface, the two WPs symmetric about the $k_z = 0$ plane are projected to the same point in the surface BZ. As they have opposite charges, each projection point contains one positive and one negative monopole charge, and there are six of such projection points. As we consider the configuration of the Fermi arcs, we note that their connection must follow the two constraints: (i) each projection point has and only has two arcs connected to it and (ii) the connection pattern should preserve both D_{3h} point group symmetry and time-reversal symmetry, which are the symmetries of the (001) surface. Based on this analysis, we find three distinct configurations for the Fermi arcs. Figure 5(a) shows the case where each projection point connects to itself via one arc. Mark that this is equivalent to no arc at all since each lobe may

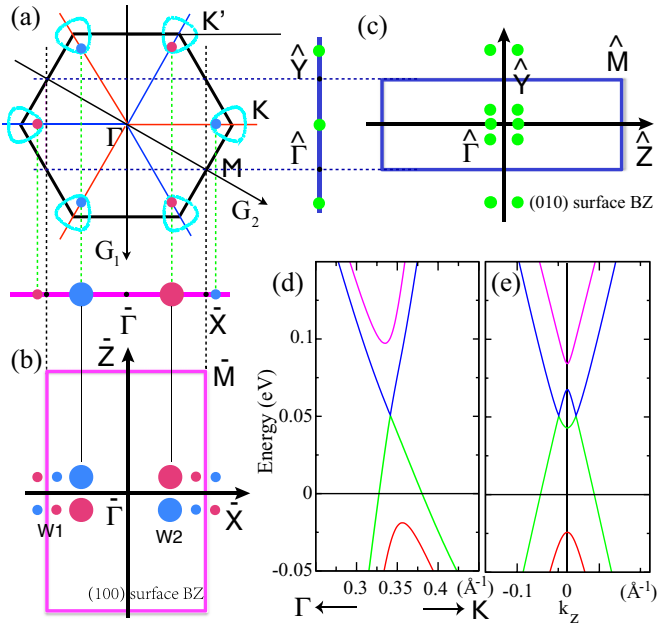


FIG. 4. (a) The node lines centering K and K' in non-SOC case and they decay into Weyl nodes when SOC is included. (b) and (c) Projections onto the (100) and (010) surface, respectively. (d) and (e) The band structures around Weyl nodes. All of the Weyl nodes are related by symmetrical operation and have the same velocity matrix and the same nodal energy about 50 meV.

shrink to a point. In Fig. 5(b) the three projection points near and symmetric about \bar{K} and \bar{K}' connect to each other in a loop, forming a trimer. In Fig. 5(c) all six projection points connect to each other in a large loop across the surface BZ, forming a hexamer. Which one of the three cases may appear in a real sample depends on the details of the surface termination and is hence not related to the bulk topology.

Based on the tight-binding model, the calculated (001)-surface states are shown in Fig. 6. The bulk states around TDNPs are projected onto area around $\bar{\Gamma}$. The projections of Weyl nodes are indicated as circles in Fig. 6(b). The band gap at 10 meV along $\bar{M}-\bar{K}$ is due to SOC and the in-gap surface bands are clearly shown in the inset of Fig. 6(a), which contributes to the single threadlike Fermi surface in Fig. 6(c) crossing $\bar{M}-\bar{K}$. When the chemical potential is set at 50 meV, exactly passing through the Weyl nodes, the Fermi arc connecting to these their projections are clearly shown in Fig. 6(d), where the $\bar{\Gamma}-\bar{K}$ path and the single threadlike Fermi arcs intersect each other. Such a connecting pattern is the trimer configuration in Fig. 5(b).

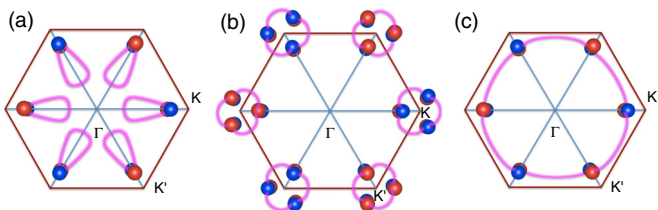


FIG. 5. The possible connection pattern of Fermi arc on ZrTe (001) surface. (a) The arc connecting to superposed Weyl points. (b) The arcs form a trimer. (c) The arcs form a hexamer.

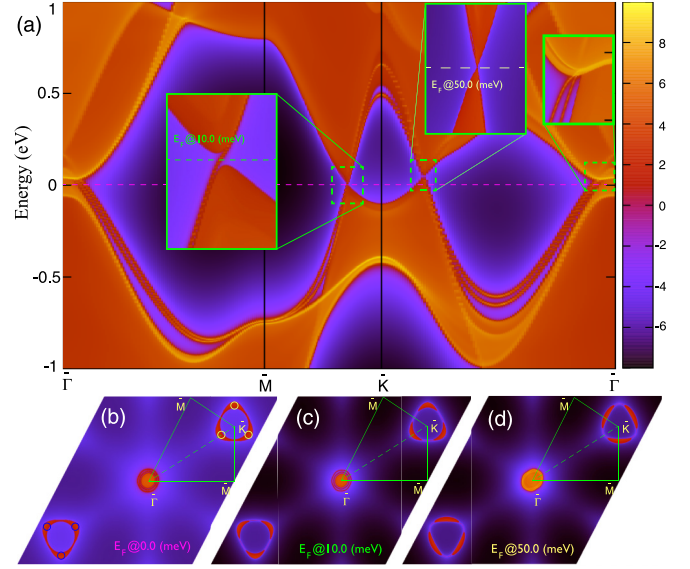


FIG. 6. ZrTe (001)-surface state. (a) The band structure weighted by the projection onto the one unit cell on the top layer. (b), (c) and (d) The Fermi surface at a chemical potential of 0, 10, and 50 meV, respectively.

IV. CONCLUSIONS

In this paper we report the simultaneous presence of triply degenerate nodal points and Weyl points in ZrTe of WC type. Due to the band inversion at K (and K') and the spin splitting, there emerge six pairs of Weyl points near K and K' in the 3D Brillouin zone. All Weyl points are related to each other via some symmetry operation from the point group D_{3h} , and hence are at the same energy level and have the same velocities. The surface states on the three low index surfaces, namely the (100), (010), and (001) surfaces, are calculated and shown. Using the (001)-surface states as an example, we show that under the same symmetry constraints, there can be topologically different patterns of how Fermi arcs connect the Weyl points. The actual pattern in a real sample depends on the conditions of the surface and hence may be tuned via surface engineering. The importance of the coexistence of TDNP and Weyl points in one material is to be revealed. One possible consequence regards the magnetoresistance, while the Weyl fermions provide for the negative magnetoresistance for magnetic field along any direction due to chiral anomaly, the “helical anomaly” [26] from the TDNP only appears when the magnetic field is along the rotation axis. Experimentally, this leads to a singularity of the magnetoresistance as a function of the field angle when it is parallel/antiparallel to the rotation axis. Another more general physical consequence is the coupling between different types of fermions, which necessitates development of new types of Fermi liquid models where three component fermions derived from TDNP couple to the two component Weyl fermions derived from the Weyl points.

Note added. Upon the completion of this work, we noticed a paper [48] that reports the triply degenerate nodal points in the same material, without studying the Weyl points therein.

ACKNOWLEDGMENTS

H.M.W., Z.F., and X.D. are supported by National Natural Science Foundation of China (Grants No. 11274359 and No. 11422428), the National 973 program of China (Grant No. 2013CB921700), the “Strategic Priority Research Program (B)” of the Chinese Academy of Sciences (Grant No. XDB07020100). H.M.W., C.F., and X.D. are supported by the National Key Research and Development Program of China under Grant No. 2016YFA0300604 (H.M.W., C.F., and X.D.), and No. 2016YFA0302400 (C.F.). Part of the calculations were performed on TianHe-1(A), the National Supercomputer Center in Tianjin, China.

APPENDIX A: (100)-SURFACE STATES

The (100)-surface states are shown in Fig. 7 with the surface band structure and Fig. 8 with the Fermi surface at different chemical potentials, namely 0.0, 10.0, and 50.0 meV. The TDNPs are projected onto the $\bar{\Gamma}$ - \bar{Z} path, which is well separated from other surface states. The surface Dirac cone at \bar{Z} is due to the $Z_2 = 1$ of the $k_z = \pi$ plane. Such a Dirac cone is clearly shown in the Fermi surface plot with a chemical potential of 10.0 meV. When the Fermi level is set to that of Weyl nodes, i.e., 50 meV, the Fermi arcs connecting the projections of Weyl nodes becomes very clear since all the Weyl nodes and the arcs are well separated from the bulk states. As shown in Figs. 8(c) and 8(d), for each W2, the projection point of two identical Weyl nodes, there are two Fermi arcs connecting it with the other one of opposite chirality. For each W1, the projection point of one Weyl node, there is only one Fermi arc connecting it. The Fermi arc passes through the path $\bar{\Gamma}$ - \bar{X} , where the $k_z = 0$ mirror plane intersects with the (100) surface. This passing through is protected by the $Z_2 = 1$ of the $k_z = 0$ plane. This is similar to the case in TaAs [12,15], where the mirror Chern number plays the role. The schematic pattern of Fermi arc is drawn in Fig. 8(e).

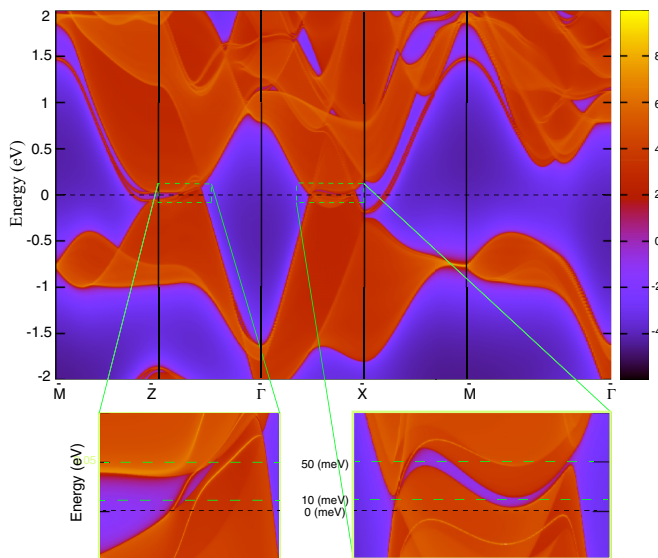


FIG. 7. ZrTe (100)-surface state with its band structure weighted by the projection onto the one unit cell on the surface layer. Part of the bands have been enlarged in the insets.

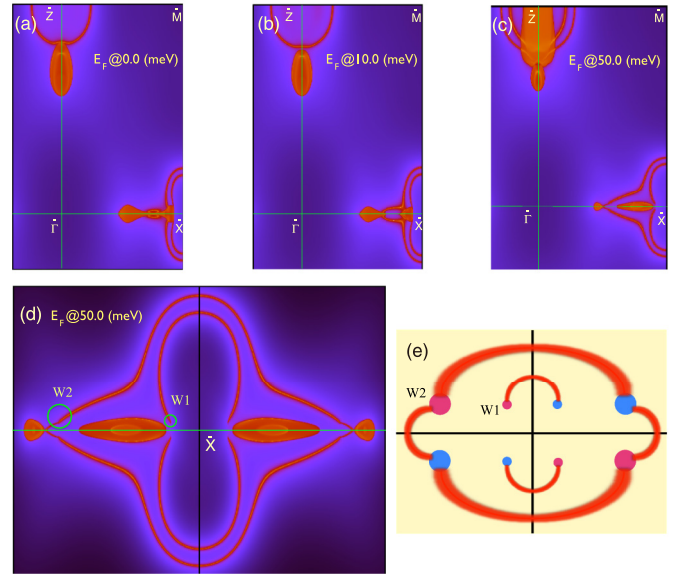


FIG. 8. Fermi surface of ZrTe (100)-surface states. (a) Chemical potential is set at 0 meV, (b) 10 meV, and (c) 50 meV. Those around \bar{X} in (c) is enlarged in (d). In (e) the Fermi arc pattern is schematically shown.

APPENDIX B: (010)-SURFACE STATES

The (010)-surface states are shown in Fig. 9. Similar to the (100) surface, the topologically nontrivial $k_z = 0$ and $k_z = \pi$ planes will intersect the surface at $\hat{\Gamma}$ - \hat{Y} and \hat{Z} - \hat{M} , respectively. There are two surface Dirac cones centering \hat{Y} and \hat{M} , respectively, seen in the surface band structure in Fig. 9(a). Along \hat{Y} - $\hat{\Gamma}$ (\hat{M} - \hat{Z}), the two branches of the surface Dirac cone connects to the valence and conduction bulk states,

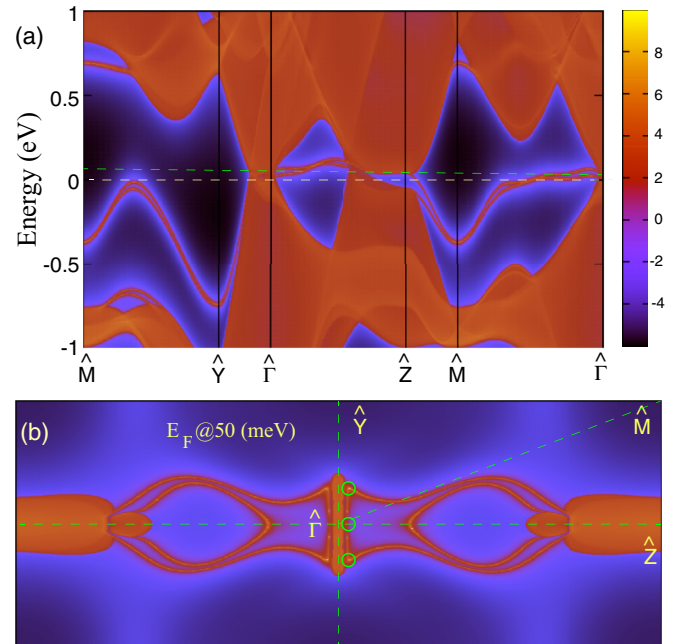


FIG. 9. ZrTe (010)-surface state. (a) The band structure weighted by the projection onto the one unit cell on the top layer. (b) The Fermi surface at 50 meV.

respectively. The two Dirac cones are connected to each other along $\hat{M}-\hat{Y}$. When setting the chemical potential at 50 meV,

the Fermi arcs connecting projections of Weyl nodes are clear, which are marked by the circles.

-
- [1] H. Weng, X. Dai, and Z. Fang, Topological semimetals predicted from first-principles calculations, *J. Phys. Condens. Matter* **28**, 303001 (2016).
- [2] C.-K. Chiu, J. C. Y. Teo, A. P. Schnyder, and S. Ryu, Classification of topological quantum matter with symmetries, *Rev. Mod. Phys.* **88**, 035005 (2016).
- [3] A. Bansil, H. Lin, and T. Das, *Colloquium*: Topological band theory, *Rev. Mod. Phys.* **88**, 021004 (2016).
- [4] S. Rao, Weyl semi-metals: A short review, [arXiv:1603.02821](https://arxiv.org/abs/1603.02821).
- [5] S. M. Young, S. Zaheer, J. C. Y. Teo, C. L. Kane, E. J. Mele, and A. M. Rappe, Dirac Semimetal in Three Dimensions, *Phys. Rev. Lett.* **108**, 140405 (2012).
- [6] Z. Wang, Y. Sun, X.-Q. Chen, C. Franchini, G. Xu, H. Weng, X. Dai, and Z. Fang, Dirac semimetal and topological phase transitions in $A_3\text{Bi}$ ($A = \text{Na, K, Rb}$), *Phys. Rev. B* **85**, 195320 (2012).
- [7] Z. Wang, H. Weng, Q. Wu, X. Dai, and Z. Fang, Three-dimensional Dirac semimetal and quantum transport in Cd_3As_2 , *Phys. Rev. B* **88**, 125427 (2013).
- [8] B. J. Yang and N. Nagaosa, Classification of stable three-dimensional Dirac semimetals with nontrivial topology, *Nat. Commun.* **5**, 4898 (2014).
- [9] S. Murakami, Phase transition between the quantum spin Hall and insulator phases in 3d: Emergence of a topological gapless phase, *New J. Phys.* **9**, 356 (2007).
- [10] X. Wan, A. M. Turner, A. Vishwanath, and S. Y. Savrasov, Topological semimetal and Fermi-arc surface states in the electronic structure of pyrochlore iridates, *Phys. Rev. B* **83**, 205101 (2011).
- [11] G. Xu, H. Weng, Z. Wang, X. Dai, and Z. Fang, Chern Semimetal and the Quantized Anomalous Hall Effect in HgCr_2Se_4 , *Phys. Rev. Lett.* **107**, 186806 (2011).
- [12] H. Weng, C. Fang, Z. Fang, B. A. Bernevig, and X. Dai, Weyl Semimetal Phase in Noncentrosymmetric Transition-Metal Monophosphides, *Phys. Rev. X* **5**, 011029 (2015).
- [13] S. M. Huang, S. Y. Xu, I. Belopolski, C. C. Lee, G. Chang, B. K. Wang, N. Alidoust, G. Bian, M. Neupane, C. Zhang, S. Jia, A. Bansil, H. Lin, and M. Z. Hasan, A Weyl Fermion semimetal with surface Fermi arcs in the transition metal monophosphide TaAs class, *Nat. Commun.* **6**, 7373 (2014).
- [14] L. Lu, Z. Wang, D. Ye, L. Ran, L. Fu, J. D. Joannopoulos, and M. Soljačić, Experimental observation of Weyl points, *Science* **349**, 622 (2015).
- [15] B. Q. Lv, H. M. Weng, B. B. Fu, X. P. Wang, H. Miao, J. Ma, P. Richard, X. C. Huang, L. X. Zhao, G. F. Chen, Z. Fang, X. Dai, T. Qian, and H. Ding, Experimental Discovery of Weyl Semimetal TaAs, *Phys. Rev. X* **5**, 031013 (2015).
- [16] B. Q. Lv, N. Xu, H. M. Weng, J. Z. Ma, P. Richard, X. C. Huang, L. X. Zhao, G. F. Chen, C. E. Matt, F. Bisti, V. N. Strocov, J. Mesot, Z. Fang, X. Dai, T. Qian, M. Shi, and H. Ding, Observation of Weyl nodes in TaAs, *Nat. Phys.* **11**, 724 (2015).
- [17] S.-Y. Xu, I. Belopolski, N. Alidoust, M. Neupane, G. Bian, C. Zhang, R. Sankar, G. Chang, Z. Yuan, C.-C. Lee, S.-M. Huang, H. Zheng, J. Ma, D. S. Sanchez, B. Wang, A. Bansil, F. Chou, P. P. Shibayev, H. Lin, S. Jia, and M. Z. Hasan, Discovery of a Weyl fermion semimetal and topological Fermi arcs, *Science* **349**, 613 (2015).
- [18] L. Yang, Z. Liu, Y. Sun, H. Peng, H. Yang, T. Zhang, B. Zhou, Y. Zhang, Y. Guo, M. Rahn, D. Prabhakaran, Z. Hussain, S.-K. Mo, C. Felser, B. Yan, and Y. Chen, Weyl semimetal phase in the non-centrosymmetric compound TaAs, *Nat. Phys.* **11**, 728 (2015).
- [19] Y. Zhang, D. Bulmash, P. Hosur, A. C. Potter, and A. Vishwanath, Quantum oscillations from generic surface Fermi arcs and bulk chiral modes in Weyl semimetals, *Sci. Rep.* **6**, 23741 (2016).
- [20] A. A. Soluyanov, D. Gresch, Z. Wang, Q. Wu, M. Troyer, X. Dai, and B. A. Bernevig, Type-II Weyl semimetals, *Nature (London)* **527**, 495 (2015).
- [21] D. T. Son and B. Z. Spivak, Chiral anomaly and classical negative magnetoresistance of Weyl metals, *Phys. Rev. B* **88**, 104412 (2013).
- [22] X. Huang, L. Zhao, Y. Long, P. Wang, D. Chen, Z. Yang, H. Liang, M. Xue, H. Weng, Z. Fang, X. Dai, and G. Chen, Observation of the Chiral-Anomaly-Induced Negative Magnetoresistance in 3D Weyl Semimetal TaAs, *Phys. Rev. X* **5**, 031023 (2015).
- [23] P. Hosur and X. Qi, Recent developments in transport phenomena in Weyl semimetals, *C. R. Phys.* **14**, 857 (2013).
- [24] B. Bradlyn, J. Cano, Z. Wang, M. G. Vergniory, C. Felser, R. J. Cava, and B. A. Bernevig, Beyond Dirac and Weyl fermions: Unconventional quasiparticles in conventional crystals, *Science* **353** (2016).
- [25] G. W. Winkler, Q. Wu, M. Troyer, P. Krogstrup, and A. A. Soluyanov, Topological Phases in $\text{InAs}_{1-x}\text{Sb}_x$: From Novel Topological Semimetal to Majorana Wire, *Phys. Rev. Lett.* **117**, 076403 (2016).
- [26] H. Weng, C. Fang, Z. Fang, and X. Dai, Topological semimetals with triply degenerate nodal points in θ -phase tantalum nitride, *Phys. Rev. B* **93**, 241202 (2016).
- [27] <http://www.openmx-square.org>
- [28] T. Ozaki and H. Kino, Numerical atomic basis orbitals from H to Kr, *Phys. Rev. B* **69**, 195113 (2004).
- [29] G. Örlýgsson and B. Harbrecht, The crystal structure of WC type ZrTe. Advantages in chemical bonding as contrasted to NiAs type ZrTe, *Z. Naturforsch. B* **54**, 1125 (2014).
- [30] G. Örlýgsson and B. Harbrecht, Structure, properties, and bonding of ZrTe (MnP type), a low-symmetry, high-temperature modification of ZrTe (WC type), *J. Am. Chem. Soc.* **123**, 4168 (2001).
- [31] J. Perdew, K. Burke, and M. Ernzerhof, Generalized Gradient Approximation Made Simple, *Phys. Rev. Lett.* **77**, 3865 (1996).
- [32] J. Heyd, G. E. Scuseria, and M. Ernzerhof, Hybrid functionals based on a screened Coulomb potential, *J. Chem. Phys.* **118**, 8207 (2003).

- [33] J. Heyd, G. E. Scuseria, and M. Ernzerhof, Erratum: Hybrid functionals based on a screened Coulomb potential [J. Chem. Phys. **118**, 8207 (2003)], *J. Chem. Phys.* **124**, 219906 (2006).
- [34] G. Kresse and J. Furthmüller, Efficiency of ab-initio total energy calculations for metals and semiconductors using a plane-wave basis set, *Comp. Mater. Sci.* **6**, 15 (1996).
- [35] G. Kresse and J. Furthmüller, Efficient iterative schemes for *ab initio* total-energy calculations using a plane-wave basis set, *Phys. Rev. B* **54**, 11169 (1996).
- [36] N. Marzari and D. Vanderbilt, Maximally localized generalized Wannier functions for composite energy bands, *Phys. Rev. B* **56**, 12847 (1997).
- [37] I. Souza, N. Marzari, and D. Vanderbilt, Maximally localized Wannier functions for entangled energy bands, *Phys. Rev. B* **65**, 035109 (2001).
- [38] H. Weng, T. Ozaki, and K. Terakura, Revisiting magnetic coupling in transition-metal-benzene complexes with maximally localized Wannier functions, *Phys. Rev. B* **79**, 235118 (2009).
- [39] H. Weng, X. Dai, and Z. Fang, Exploration and prediction of topological electronic materials based on first-principles calculations, *MRS Bull.* **39**, 849 (2014).
- [40] H. Weng, R. Yu, X. Hu, X. Dai, and Z. Fang, Quantum anomalous Hall effect and related topological electronic states, *Adv. Phys.* **64**, 227 (2015).
- [41] A. Friedrich, W. Morgenroth, L. Bayarjargal, E. A. Juarez-Arellano, B. Winkler, and Z. Konôpková, *In situ* study of the high pressure high-temperature stability field of TaN and of the compressibilities of θ -TaN and TaON, *High Press. Res.* **33**, 633 (2013).
- [42] G. Brauer, E. Mohr, A. Neuhaus, and A. Skokan, θ -TaN, eine Hochdruckform von Tantalnitrid, *Monatsh. Chem.* **103**, 794 (1972).
- [43] L. B. Litinskii, The band structure of hexagonal NbN, *Solid State Commun.* **71**, 299 (1989).
- [44] L. B. Litinsky, On Fermi's surfaces of hexagonal carbides and nitrides, *Solid State Commun.* **75**, 1009 (1990).
- [45] R. Yu, X. L. Qi, A. Bernevig, Z. Fang, and X. Dai, Equivalent expression of Z_2 topological invariant for band insulators using the non-Abelian Berry connection, *Phys. Rev. B* **84**, 075119 (2011).
- [46] J. Ruan, S.-K. Jian, H. Yao, H. Zhang, S.-C. Zhang, and D. Xing, Symmetry-protected ideal Weyl semimetal in HgTe-class materials, *Nat. Commun.* **7**, 11136 (2016).
- [47] J. Ruan, S.-K. Jian, D. Zhang, H. Yao, H. Zhang, S.-C. Zhang, and D. Xing, Ideal Weyl Semimetals in the Chalcopyrites CuTlSe₂, AgTlTe₂, AuTlTe₂, and ZnPbAs₂, *Phys. Rev. Lett.* **116**, 226801 (2016).
- [48] Z. Zhu, G. W. Winkler, Q. S. Wu, J. Li, and A. A. Soluyanov, Triple Point Topological Metals, *Phys. Rev. X* **6**, 031003 (2016).